



Cite this: DOI: 10.1039/c9cp06372b

Anomalous proton conduction behavior across a nanoporous two-dimensional conjugated aromatic polymer membrane†

 Le Shi, *^a Zhixuan Ying,^a Ao Xu ^b and Yonghong Cheng^a

We investigate aqueous proton penetration behavior across a newly synthesized nanoporous two-dimensional conjugated aromatic polymer (2D-CAP) membrane using extensive ReaxFF reactive molecular dynamics simulations. We found that the proton penetration energy barrier across 2D-CAP is twice as high as that of graphtetrayne, even though 2D-CAP exhibits a larger pore size. Detailed analysis indicates that the anomalous high proton conduction energy barrier of 2D-CAP originates from its unique atomic nanopore structure. The hydrogen atoms at the periphery of the 2D-CAP nanopores can form a stable local hydrogen bond network with water molecules inside or surrounding the nanopores. The mobility of water molecules involved in this local hydrogen bond network will be significantly lowered, and the proton transportation process across the nanopores will thus be impeded. Our results show that the proton penetration behavior across nanoporous 2D materials is influenced not only by the pore size, but also by the decorated atoms or functional groups at the pore edges. Hydrogen atoms at the periphery of nanopores with certain geometry can form a stable local hydrogen bond network with neighboring water molecules, further hampering the proton conductivity.

 Received 25th November 2019,
 Accepted 20th December 2019

DOI: 10.1039/c9cp06372b

rsc.li/pccp

1. Introduction

Proton exchange membranes play a critical role in the development of energy conversion and storage systems such as fuel cells,^{1,2} flow batteries^{3,4} and electrolyzers.⁵ The conventional polymer-based membranes including Nafion,⁶ poly-benzimidazole⁷ and sulfonated polyether-ether ketones⁸ suffer from various issues such as crossover of active species, low proton conductivity and poor stability. A proton exchange membrane that can simultaneously provide high proton conductivity, satisfactory selectivity and good stability is urgently needed.

Recently, a new type of membrane based on nanoporous two-dimensional (2D) materials has attracted lots of attention from various communities.^{9–12} By utilizing the intrinsic pores or creating nanoscale pores in 2D materials, selective mass conduction can be achieved. The atomic thickness makes this kind of membrane the thinnest barrier, which is expected to enable high permeance. Meanwhile, by controlling the pore size, ultrahigh selectivity of the membrane can be obtained. Many theoretical and experimental efforts have been devoted to

the development of nanoporous 2D membranes for applications in gas separation,^{13–15} water desalination,^{16–18} and so on. In 2014, Geim *et al.* proposed for the first time that protons can conduct across the atomic pores formed by the electron clouds of graphene and h-BN.¹⁹ As the atomic pore sizes of these 2D materials are too small to allow the penetration of any other species, ultrahigh selectivity of the 2D materials can be achieved. Their work opened up a new avenue for the design of next-generation proton exchange membranes. Afterwards, many researchers investigated the aqueous proton conduction behavior across nanoporous 2D materials.^{20–27} In our previous work, we explored the effect of 2D graphyne pore size on proton conduction behavior. We found that when the pore size is large enough, water molecules can penetrate the nanopores and form “water wires” across the 2D materials, which provide a highway for proton conduction *via* the Grotthuss mechanism.²² Among all the explored pore sizes, graphtetrayne with four acetylenic linkages on each side of the triangular pores (G4),²⁸ as shown in Fig. 1(b), exhibits the highest proton conductivity as well as promising selectivity due to its relatively large pore size and patterned aqueous/vacuum interphase in an aqueous environment. In 2017, Loh *et al.* synthesized a 2D conjugated aromatic polymer (2D-CAP) *via* C–C coupling reactions between tetrabromopolyaromatic monomers, as shown in Fig. 1(a).²⁹ Follow-up molecular dynamics (MD) simulations indicated that this nanoporous 2D material can serve as a new type of water desalination membrane with an ultrahigh water flux.³⁰ As its

^a State key Laboratory of Electrical Insulation and Power Equipment,

 Center of Nanomaterials for Renewable Energy, School of Electrical Engineering,
 Xi'an Jiaotong University, Xi'an 710049, China. E-mail: le.shi@mail.xjtu.edu.cn

^b School of Aeronautics, Northwestern Polytechnical University, Xi'an 710072, China

† Electronic supplementary information (ESI) available. See DOI: 10.1039/c9cp06372b

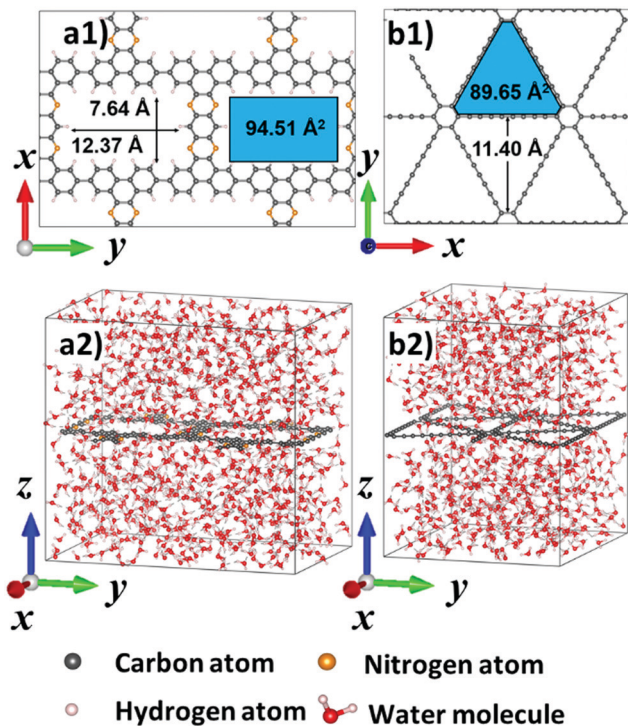


Fig. 1 Atomic structure of (a) 2D-CAP and (b) G4 in a vacuum and aqueous environment.

nanoscale pore size is slightly larger than that of G4, a comparable or even higher proton conductivity is expected, which would provide a new choice for the future design of next-generation membranes.

In this work, we explored the aqueous proton conduction capability of 2D-CAP using extensive reactive force field (ReaxFF) MD simulations. Surprisingly, it is found that though it has a larger pore size, the proton conduction energy barrier of 2D-CAP ($5.56 \pm 0.23 \text{ kcal mol}^{-1}$) is twice as high as that of G4 ($2.55 \pm 0.41 \text{ kcal mol}^{-1}$). Further analysis on the surrounding water structure shows that the hydrogen atoms at the periphery of the nanopores of 2D-CAP can form a stable local hydrogen bond network with surrounding water molecules. This local hydrogen bond network can restrain the movement of involved water molecules, therefore impeding the proton conduction process. Our results reveal that the proton conduction capability of nanoporous 2D materials not only depends on the pore size, but is also significantly influenced by the decoration atoms or functional groups at the pore edges.

2. Computational methods

2.1 Density functional theory (DFT) calculations

The atomic structures of 2D-CAP and G4 were taken from previous reports,^{28,29} and further optimized using the Abinit software package.^{31–33} The Perdew–Burke–Ernzerhof (PBE) generalized gradient approximation (GGA)³⁴ together with the projector-augmented-wave (PAW) method³⁵ was adopted to describe the exchange correlation functional and the electron–ion interaction.

The cutoff energy was set to be 20 Ha, and the k -point mesh was set to be $<0.05 \text{ \AA}^{-1}$. A force tolerance of 0.01 eV \AA^{-1} was adopted for the geometry optimization process.

2.2 ReaxFF MD simulations

The recently developed CHON-2017_weak ReaxFF force field parameters^{36,37} were used for all the reactive MD simulations to accurately describe the weak interaction of functionalized hydrocarbon/water molecules in the condensed phase and capture the Grotthuss hopping proton motion.^{38,39} Detailed validation of the CHON-2017-weak force field has been carried out by Zhang *et al.*,^{36,37} including water density, water/hydronium ion self-diffusion coefficient, radial distribution function, IR spectra, Raman spectra, proton diffusion constant *etc.*, all of which agree well with the experimental results. We also calculated the water density and water self-diffusion constant at 300 K based on a cubic simulation system containing 267 water molecules. The simulation results are shown in Table S1 and Fig. S1 (ESI†), which show good consistency with the experimental work. All MD simulations were performed using LAMMPS^{40,41} software. For all the production ReaxFF MD simulations, the time step was set to be 0.25 fs and the Nosé–Hoover chain thermostat was used. The pressure and temperature damping constant was set to be 1000 and 100 fs for the NPT and NVT MD simulations, respectively. For metadynamics⁴² simulations, the PLUMED plugin⁴³ was used to deal with the proton hopping process. As protons mainly exist in the form of hydronium ions in aqueous systems, the distance L between the oxygen atom in the hydronium ion $r_{\text{O}}(t)$ and the 2D-CAP was defined as the collective variable (CV):^{22,44,45}

$$L = r_{\text{O}}(z) - Z_{\text{2D-CAP}} \quad (1)$$

where $Z_{\text{2D-CAP}}$ is the position of the 2D material in the z direction, and $r_{\text{O}}(z)$ can be calculated using:

$$r_{\text{O}}(z) = \frac{\sum_{i \in \{\text{O}_w\}} z_i e^{\lambda n_i}}{\sum_{i \in \{\text{O}_w\}} e^{\lambda n_i}} \quad (2)$$

where z_i is the z position of the water's or hydronium's oxygen i , λ is a large number (we set as 100 in our computation), and $\{\text{O}_w\}$ refers to all oxygen atoms in the simulation system. The variable n_i is the hydrogen coordination number:

$$n_i = \sum_{j \in \{H_w\}} n(r_{ij}) \quad (3)$$

where $n(r_{ij})$ was determined by a switching function

$$n(r_{ij}) = \frac{1 - \left(\frac{r_{ij}}{r_c}\right)^6}{1 - \left(\frac{r_{ij}}{r_c}\right)^{12}}, \quad r_{ij} \text{ is the distance between oxygen atom } i$$

and hydrogen atom j , and $\{H_w\}$ refers to all hydrogen atoms in the simulation system. The cutoff radius r_c is set to be 1.25 \AA . The variable n_i is very close to 3 when i is the oxygen atom of the hydronium ion and 2 in the case of a water molecule. With the exponential weight factor $e^{\lambda n_i}$, the $r_{\text{O}}(z)$ value calculated will be very close to the z value of the hydronium ion.

In metadynamics simulations, the Gaussian hills were deposited every 100 MD steps. The height and width of Gaussian hills were $0.02 \text{ kcal mol}^{-1}$ and 0.5 \AA , respectively. The atomic coordinates were recorded every 100 simulation steps (25 fs) to analyze water dynamics and proton transfer behavior. To test the influence of sampling rate on the statistical results of proton position, we performed a 500 ps ReaxFF MD simulation in the *NVT* ensemble for a box with a side length of 12.4 \AA containing 64 water molecules and an extra proton, as shown in Fig. S2 (ESI[†]). The trajectory of the proton was sampled every 1, 10, 100 and 1000 steps, and the comparison is shown in Fig. S3 (ESI[†]). It can be found that for the probability distribution of the proton position along the *x* direction, as shown in Fig. S3(b) (ESI[†]), the results obtained from sampling rates of 1, 10, and 100 steps agree well with each other. Another 500 ps ReaxFF MD simulation with a similar simulation setup without an extra proton was performed to test the influence of sampling rate on the angle distribution of water. Fig. S4(a) (ESI[†]) shows the angle of one water molecule as a function of simulation time. It can be found that the timescale for water dipole orientational dynamics is about 0.1 ps. Fig. S4(b) (ESI[†]) shows that the statistical results obtained from sampling rates of 1, 10, 100 steps agree well with each other.

3. Results and discussion

3.1 Proton conduction behavior across 2D-CAP and G4 membrane

The simulation systems were based on a $2.4 \times 3.5 \text{ nm}$ 2D-CAP sheet and a $2.9 \times 2.5 \text{ nm}$ G4 sheet, as shown in Fig. 1. The 2D materials were put into a periodic aqueous box with the initial height of 3.0 nm and water density of 1 g cm^{-3} , respectively, and then underwent a 2 ns ReaxFF MD simulation in the *NPT* ensemble ($P = 1 \text{ atm}$, $T = 300 \text{ K}$) with *x* and *y* directions fixed to decide the box size at equilibrium. The system configurations after the *NPT* equilibration are listed in Table S3 (ESI[†]). Afterwards, the systems were further equilibrated in the *NVT* ensemble ($T = 300 \text{ K}$) for another 2 ns. All production runs were performed in the *NVT* ensemble for the ease of data

analysis. First, the systems with 2D materials fully relaxed were studied. The snapshots of *NVT* simulations can be found in Fig. S5 (ESI[†]), where the 2D material structure fluctuates in the aqueous environment. The fluctuation of 2D materials makes it difficult to calculate the precise relative distance between water/proton and membrane, as well as difficult to analyze the water/proton distribution. Thus, unless otherwise specified, the position of 2D materials was fixed in the following production runs.

To study the proton transportation behavior, we put one extra proton in each aqueous system. The distance between the proton and 2D materials as a function of time is shown in Fig. 2, which is consistent with our previous *ab initio* molecular dynamics (AIMD) simulation results²² that spontaneous proton penetration occurs frequently in a G4 system. However, for the 2D-CAP system, the situations are unexpected. It can be found that in the 2D-CAP system, no spontaneous proton penetration behavior occurred, and there exists an area with a height about 2 \AA where no proton appeared during the entire simulation time. This phenomenon indicates that proton penetration across 2D-CAP is much harder than across G4, which is in contrast to the straightforward understanding that larger pores correspond to higher proton conductivity. Fig. S6 (ESI[†]) shows the distance between proton and 2D materials as a function of simulation time with 2D materials fully relaxed. The general trends agree well with the cases in which 2D materials were fixed (as shown in Fig. 2), where spontaneous proton penetration across G4 occurred, while no proton penetration across 2D-CAP has been observed.

To quantitatively calculate the proton penetration energy barriers, we performed metadynamics simulations for the case of 2D-CAP, and unbiased MD simulations for the case of G4. The metadynamics setup is shown in Fig. S7 (ESI[†]). For unbiased MD simulations, the free energy was calculated as:⁴⁶

$$F(z) = -k_{\text{B}}T \ln[P(z)] \quad (4)$$

where *z* is the position of the hydronium ion in the *z* direction, and *P*(*z*) is the probability that the hydronium ion appears in a certain *z* area in a simulation time of 2 ns.

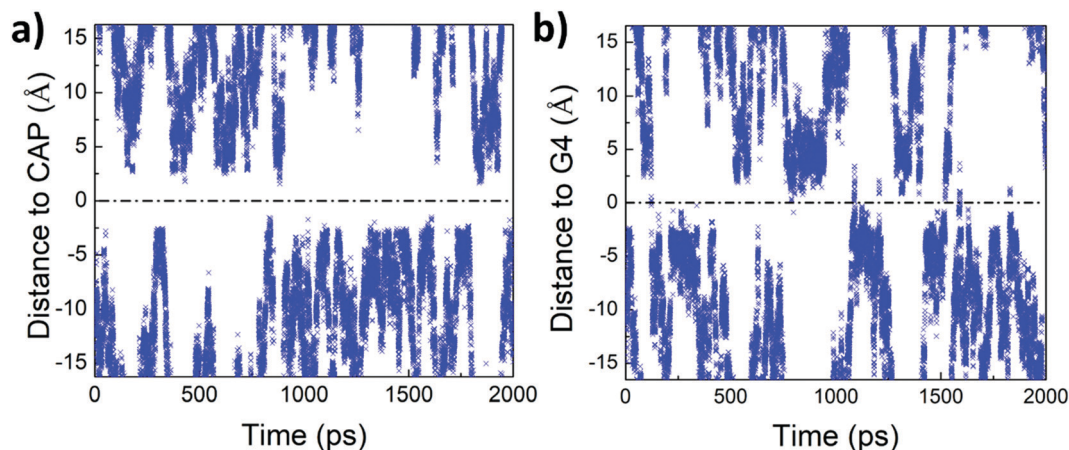


Fig. 2 Distance between proton and (a) 2D-CAP and (b) G4 as a function of time in unbiased ReaxFF molecular dynamics simulation for 2 ns.

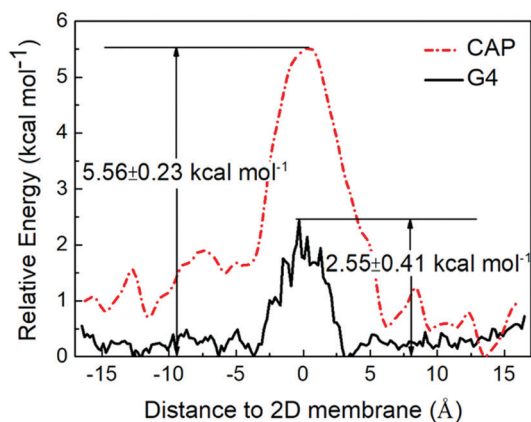


Fig. 3 Energy profiles of proton as a function of the distance to the 2D membrane.

For each system, three simulations with different initial geometries were performed. The calculated energy barriers for each case are listed in Tables S5 and S6 (ESI[†]). The detailed proton trajectories and energy profiles for each case can be found in Fig. S8–S19 (ESI[†]). As shown in Fig. 3, the proton penetration energy barrier across G4 is 2.55 ± 0.41 kcal mol⁻¹, while the proton penetration energy barrier across 2D-CAP is 5.56 ± 0.23 kcal mol⁻¹, which is twice as high as that of G4. As fluctuation enhances the relative movement between the 2D membrane and neighboring water molecules, we propose that the fluctuation may facilitate the proton penetration process and result in a lower proton penetration energy barrier.

3.2 Water density analysis

To understand the reason for the anomalously high proton penetration energy barrier of 2D-CAP, we analyzed the water distribution surrounding the 2D materials. From Fig. 4, it can be found that a water layering effect exists in both cases.^{47,48} For 2D-CAP, the layering effect is more significant with higher water density peaks near the 2D material. Abnormally, for 2D-CAP, there exists an extra peak just at the position of the 2D material. The peak value is as high as 1.67 g cm⁻³, which is

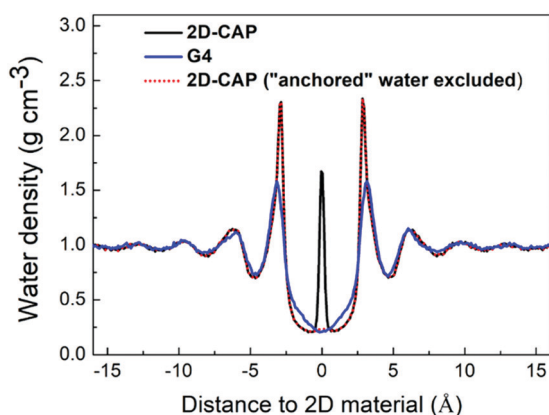


Fig. 4 Water density as a function of the distance to 2D materials.

even higher than the bulk water density where no 2D material exists.

To explain this abnormal water density peak, we analyzed the x - y slice of the time-averaged three-dimensional water density at z corresponding to the 2D material position. A 2 Å thick slab around the 2D material was considered, as shown in Fig. S20(a) (ESI[†]). The detailed density value was calculated based on a mesh grid, as shown in Fig. S20(b) (ESI[†]), with a mesh size of 0.25 Å as:

$$\rho(x, y) = \frac{M \sum_{i=1}^{N_{\text{frame}}} n_i}{N_A \Delta x \Delta y \Delta z N_{\text{frame}}} \quad (5)$$

where M is the mass for 1 mole of water, N_A is the Avogadro constant, n_i is the number of water molecules found inside the grid at frame i , and N_{frame} is the number of frames considered. The value of Δx and Δy was set to be 0.25 Å, and Δz was set to be 2 Å. From Fig. 5(a) and (b), it can be found that there exist some “hot spots” in the case of 2D-CAP, where the water density exceeds 5 g cm⁻³. These “hot spots” cannot be observed in the case of G4. Fig. 5(c) shows the water density distribution of 2D-CAP with a larger density scale. It is shown that the “hot spots” in Fig. 5(a) can be classified into two categories. The first category is the “hot spots” in black circles, where the water density reaches higher than 35 g cm⁻³; and the second category is the “hot spots” in black squares, where the water density falls in a much lower range of 5 – 10 g cm⁻³.

To further explore the origin of these hot spots, we analyzed the snapshots during MD simulations. As shown in Fig. 6(a), for all the snapshots analyzed, the areas highlighted by the green and black circles always contain a water molecule, which agrees well with the “hot spots” in Fig. 5(c) where water density reaches higher than 35 g cm⁻³. The specific atomic structure of hydrogen atoms decorating the nanopores inherited from the precursor tetrabromopolyaromatic monomer²⁹ (as shown in the black rectangle in Fig. S21, ESI[†]) enables the formation of two stable hydrogen bonds between water molecules and hydrogen atoms highlighted in blue color in Fig. 6(a). This phenomenon is similar with the hydration sites of biomolecules such as proteins and DNA.^{49–51} A detailed analysis of the atomic coordinates of the water oxygen atoms residing in the green circles, as shown in Fig. 6(c), shows that these water molecules never changed their position during the entire simulation time of 1 ns, as if being “anchored” to the corners of the nanopores. This “anchoring effect” can also be observed in simulations with 2D-CAP fully relaxed, as shown in Fig. S22 (ESI[†]). When calculating the water density, these spots contribute a high density value. As shown in Fig. 4, exclusion of these “anchored” water molecules results in the disappearance of the abnormal peak, while the residue displays a water density distribution similar to that of G4. The interaction between water molecules and G4 is much weaker, and no formed bond can be observed, as shown in Fig. 6(b).

The Grotthuss proton transport mechanism involves proton relay among different water molecules, where water molecule rotation plays an important role. In Fig. 6(d), we compared the

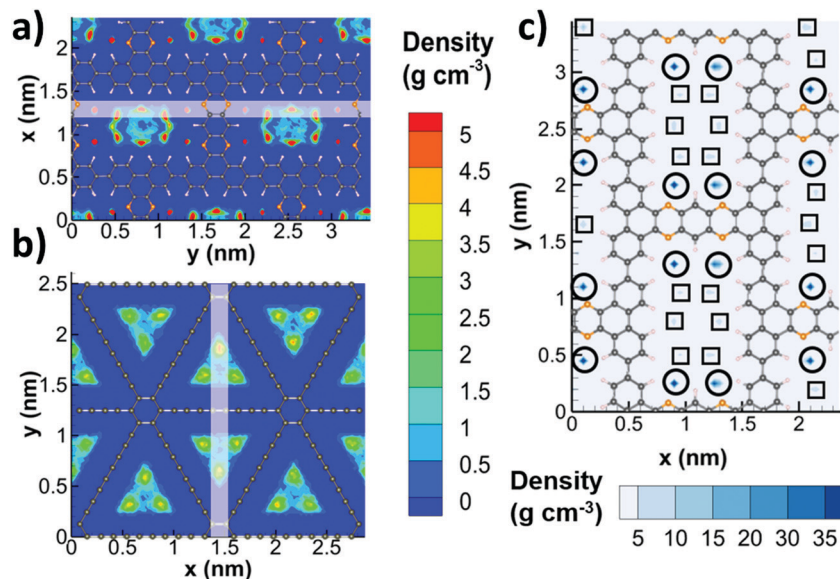


Fig. 5 x - y slice of the time-averaged three-dimensional water density at z corresponding to the (a) 2D-CAP and (b) G4 membrane. The white ribbons indicate the area involved in the further y - z slice. (c) x - y slice of the time-averaged three-dimensional water density at z corresponding to the 2D-CAP membrane with enlarged density scale.

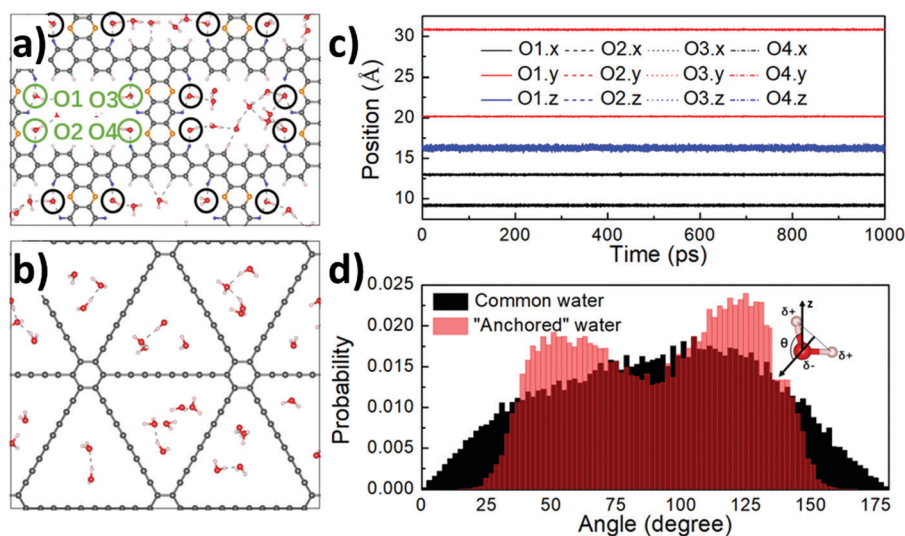


Fig. 6 (a) Snapshot of 2D-CAP in an aqueous environment. The black and green circles denote the “anchored” water molecules. (b) Snapshot of G4 in an aqueous environment. (c) Position of the “anchored” water molecules in green circles as a function of simulation time. (d) Angle distribution for an “anchored” water and a common water molecule during 1 ns simulation time.

distribution of water dipole direction of the “anchored” water molecules with common water molecules during 1 ns MD simulation. The water dipole angle is defined as the angle between the water dipole moment and z axis, as shown in the inset of Fig. 6(d). It can be found that the water dipole direction distribution of “anchored” water molecules is visibly different from that of common water molecules, and the “anchored” water molecule cannot rotate to the directions where the dipole angle lies between 0–20 and 160–180 degree. The hydrogen atoms in these “anchored” water molecules together with the other hydrogen atoms at the periphery of the nanopores (pink

hydrogen atoms, as shown in Fig. 6(a)) can form a local hydrogen bond network with neighboring water molecules. The relative position between “anchored” water molecules and the hydrogen atoms at the periphery of nanopores will fluctuate around a fixed value, as shown in Fig. S22 (ESI[†]), and the geometry of the formed local hydrogen bond network will be restrained. Water molecules inside or surrounding the nanopores will tend to appear in the position where a stable hydrogen bond network can be formed to lower the free energy of the system, which contributes to the formation of the “hot spots” indicated by black squares in Fig. 5(c) with a water density of 5–10 g cm^{-3} .

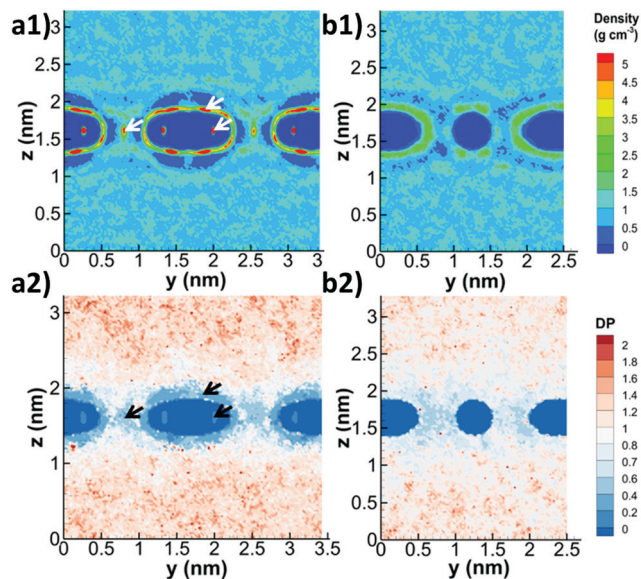


Fig. 7 y - z slice of the time-averaged three-dimensional water density at x , as illustrated in Fig. 5, for (a1) 2D-CAP and (b1) G4. y - z slice of the dynamical propensity ($t = 5$ ps) at x , as illustrated in Fig. 5, for (a2) 2D-CAP and (b2) G4. The white and black arrows indicate the area with high water density and low dynamical propensity.

3.3 Dynamical propensity analysis

Based on the above results, we propose that the hydrogen atoms decorating the edges of 2D-CAP nanopores can result in the formation of a stable local hydrogen bond network, which will restrain the movement of involved water molecules, thus impeding the proton penetration behavior and leading to a relatively higher proton penetration energy barrier. To verify our hypothesis, we calculated the dynamical propensity (DP) distribution of 2D-CAP and G4 systems, respectively. The DP for a certain water molecule was calculated as:

$$DP_i = \left\langle \frac{\|\mathbf{r}_i(t + t_0) - \mathbf{r}_i(t)\|^2}{\text{MSD}} \right\rangle \quad (6)$$

where $\mathbf{r}_i(t)$ is the position of water oxygen atom i at time t , and MSD is the mean square displacement of all water oxygen atoms in this system. t_0 is the evolution time used to characterize DP. This method has been widely used to characterize the dynamical heterogeneity of certain atomic structures, where the DP value was obtained by averaging over different trajectories that start from the same initial geometry, but with a different set of velocities (so called iso-configurational analysis).^{52–55} In our situation, rather than the dynamical heterogeneity induced by the specific atomic configuration, the dynamical heterogeneity induced by the existence of a 2D material is needed. In our calculations, we averaged the DP value over different water initial geometries to exclude the influence of a specific water arrangement. The DP values were collected and analyzed based on the initial positions of the studied water molecules. The MSD calculated for 2D-CAP and G4 systems is plotted in Fig. S24 (ESI†). Different t_0 values were tested including 1 ps, 3 ps, 5 ps, 10 ps, 20 ps, 50 ps and 100 ps to choose the t_0 that could maximize the

heterogeneity. To highlight the influence of the stable local hydrogen bond network, we analyzed the y - z slice of the DP at x , as indicated by the white ribbons in Fig. 5, where the “hot spots” were covered. The DP results with different t_0 are shown in Fig. S25–S31 (ESI†). It can be found that for t_0 between 1 ps and 20 ps, the DP distribution patterns are quite similar, and a longer time corresponds to a more homogeneous distribution. When t_0 reaches 50–100 ps, the time is long enough for the water molecules to migrate to a position faraway and the dynamical heterogeneity will become obscure.

Fig. 7 shows the water density as well as the DP distribution for both the 2D-CAP and G4 systems. From Fig. 7(a1) and (b1), it can be found that similar to Fig. 5(a) and (b), unique “hot spots” as indicated by the white arrows can be observed for the 2D-CAP case. The distribution of “hot spots” is three dimensional and not limited to the 2D plane of the 2D material, which agrees well with the geometrical characteristics of a hydrogen bond network. The dynamical propensity distribution illustrates the spatial range of the stable local hydrogen bond network in the case of 2D-CAP. As a comparison, the water density distribution surrounding G4 is much more homogeneous, only a slight segregation effect can be observed up to about 2 Å away from the 2D membrane. Fig. 7(a2) and (b2) shows the DP distribution with $t_0 = 5$ ps. It can be found that for 2D-CAP, the water density distribution and DP distribution reveal a strong correlation. As indicated by the black arrows in Fig. 7(a2), the positions with high water density correspond to low DP, which indicates a low mobility of water molecules in this area. While for G4, a similar correlation cannot be found. This obvious correlation verified our hypothesis that the stable local hydrogen bond network formed between the hydrogen atoms at the periphery of 2D-CAP nanopores and water molecules can restrain the movement of involved water molecules, thus impeding the proton Grothuss transportation process and resulting in a higher proton penetration energy barrier.

4. Conclusion

In this work, we explored the proton penetration behavior across a newly synthesized nanoporous 2D material, namely 2D-CAP, and compared its proton conduction capability with another 2D material, G4. Surprisingly, though with a larger pore size, the proton conduction energy barrier across 2D-CAP is twice as high as that of G4. Detailed analysis on water density and dynamical heterogeneity distribution implies that the hydrogen atoms at the periphery of the nanopores of 2D-CAP can form a stable local hydrogen bond network with neighboring water molecules. The local hydrogen bond network can restrain the movement of involved water molecules and further impede the proton transportation process, therefore resulting in a higher proton penetration energy barrier. Our study shows that in addition to the pore size, the decoration functional groups of nanopores also play important roles in determining the proton conduction capability. For some cases like 2D-CAP, the decorated hydrogen atoms can impede the proton conduction process. Our results provide

insight into the proton conduction behavior across 2D materials, and shed light for future design of next-generation proton exchange membranes.

Conflicts of interest

There are no conflicts to declare.

Acknowledgements

The work described in this paper was supported by the National Natural Science Foundation of China (51907159) and Young Talent Recruiting Plans of Xi'an Jiaotong University (DQ6J002). The simulations were carried out at LvLiang Cloud Computing Center of China, and were performed on TianHe-2.

Notes and references

- S. J. Peighambardoust, S. Rowshanzamir and M. Amjadi, *Int. J. Hydrogen Energy*, 2010, **35**, 9349–9384.
- S. Bose, T. Kuila, T. X. H. Nguyen, N. H. Kim, K. T. Lau and J. H. Lee, *Prog. Polym. Sci.*, 2011, **36**, 813–843.
- X. Li, H. Zhang, Z. Mai, H. Zhang and I. Vankelecom, *Energy Environ. Sci.*, 2011, **4**, 1147–1160.
- A. Xu, W. Shyy and T. Zhao, *Acta Mech. Sin.*, 2017, **33**, 555–574.
- Q. Feng, G. Liu, B. Wei, Z. Zhang, H. Li and H. Wang, *J. Power Sources*, 2017, **366**, 33–55.
- K. A. Mauritz and R. B. Moore, *Chem. Rev.*, 2004, **104**, 4535–4586.
- P. Staiti, F. Lufano, A. S. Arico, E. Passalacqua and V. Antonucci, *J. Membr. Sci.*, 2001, **188**, 71–78.
- L. Li, J. Zhang and Y. Wang, *J. Membr. Sci.*, 2003, **226**, 159–167.
- L. Wang, M. S. Boutilier, P. R. Kidambi, D. Jang, N. G. Hadjicostantinou and R. Karnik, *Nat. Nanotechnol.*, 2017, **12**, 509.
- B. Mi, *Science*, 2019, **364**, 1033–1034.
- L. Prozorovska and P. R. Kidambi, *Adv. Mater.*, 2018, **30**, 1801179.
- G. Liu, W. Jin and N. Xu, *Angew. Chem., Int. Ed.*, 2016, **55**, 13384–13397.
- H. Li, Z. Song, X. Zhang, Y. Huang, S. Li, Y. Mao, H. J. Plohn, Y. Bao and M. Yu, *Science*, 2013, **342**, 95–98.
- S. W. Cranford and M. J. Buehler, *Nanoscale*, 2012, **4**, 4587–4593.
- Y. Tao, Q. Xue, Z. Liu, M. Shan, C. Ling, T. Wu and X. Li, *ACS Appl. Mater. Interfaces*, 2014, **6**, 8048–8058.
- S. P. Surwade, S. N. Smirnov, I. V. Vlassiuk, R. R. Unocic, G. M. Veith, S. Dai and S. M. Mahurin, *Nat. Nanotechnol.*, 2015, **10**, 459.
- S. Dervin, D. D. Dionysiou and S. C. Pillai, *Nanoscale*, 2016, **8**, 15115–15131.
- M. Heiranian, A. B. Farimani and N. R. Aluru, *Nat. Commun.*, 2015, **6**, 8616.
- S. Hu, M. Lozada-Hidalgo, F. C. Wang, A. Mishchenko, F. Schedin, R. R. Nair, E. W. Hill, D. W. Boukhvalov, M. I. Katsnelson and R. A. W. Dryfe, *et al.*, *Nature*, 2014, **516**, 227.
- X. H. Yan, R. Wu, J. B. Xu, Z. Luo and T. S. Zhao, *J. Power Sources*, 2016, **311**, 188–194.
- L. Shi, A. Xu, G. H. Chen and T. S. Zhao, *J. Phys. Chem. Lett.*, 2017, **8**, 4354–4361.
- L. Shi, A. Xu, D. Pan and T. S. Zhao, *Nat. Commun.*, 2019, **10**, 1165.
- J. Xu, H. Jiang, Y. Shen, X. Z. Li, E. G. Wang and S. Meng, *Nat. Commun.*, 2019, **10**, 1–8.
- J. L. Achtyl, R. R. Unocic, L. Xu, Y. Cai, M. Raju, W. Zhang, R. L. Sacci, I. V. Vlassiuk, P. F. Fulvio and P. Ganesh, *et al.*, *Nat. Commun.*, 2015, **6**, 6539.
- S. M. Holmes, P. Balakrishnan, V. S. Kalangi, X. Zhang, M. Lozada-Hidalgo, P. M. Ajayan and R. R. Nair, *Adv. Energy Mater.*, 2017, **7**, 1601216.
- M. I. Walker, P. Braeuninger-Weimer, R. S. Weatherup, S. Hofmann and U. F. Keyser, *Appl. Phys. Lett.*, 2015, **107**, 213104.
- L. Shi, A. Xu and Y. H. Cheng, *J. Phys. Chem. C*, 2019, **123**, 27429–27435.
- J. Gao, J. Li, Y. Chen, Z. Zuo, Y. Li, H. Liu and Y. Li, *Nano Energy*, 2018, **43**, 192–199.
- W. Liu, X. Luo, Y. Bao, Y. P. Liu, G. H. Ning, I. Abdelwahab, L. Li, C. T. Nai, Z. G. Hu and D. Zhao, *et al.*, *Nat. Chem.*, 2017, **9**, 563.
- Y. G. Yan, W. S. Wang, W. Li, K. P. Loh and J. Zhang, *Nanoscale*, 2017, **9**, 18951–18958.
- X. Gonze, J. M. Beuken, R. Caracas, F. Detraux, M. Fuchs, G. M. Rignanese, L. Sindic, M. Verstraete, G. Zerah and F. Jollet, *et al.*, *Comput. Mater. Sci.*, 2002, **25**, 478–492.
- X. Gonze, B. Amadon, P. M. Anglade, J. M. Beuken, F. Bottin, P. Boulanger, F. Bruneval, D. Caliste, R. Caracas and M. Cote, *et al.*, *Comput. Phys. Commun.*, 2009, **180**, 2582–2615.
- X. Gonze, *Z. Kristallogr.*, 2005, **220**, 558–562.
- J. P. Perdew, M. Ernzerhof and K. Burke, *J. Chem. Phys.*, 1996, **105**, 9982–9985.
- P. E. Blöchl, *Phys. Rev. B: Condens. Matter Mater. Phys.*, 1994, **50**, 17953.
- W. Zhang and A. C. Van Duin, *J. Phys. Chem. B*, 2018, **122**, 4083–4092.
- W. Zhang, X. Chen and A. C. Van Duin, *J. Phys. Chem. Lett.*, 2018, **9**, 5445–5452.
- A. Hassanali, F. Giberti, J. Cuny, T. D. Kühne and M. Parrinello, *Proc. Natl. Acad. Sci. U. S. A.*, 2013, **110**, 13723–13728.
- D. Marx, *ChemPhysChem*, 2006, **7**, 1848–1870.
- S. Plimpton, *J. Comput. Phys.*, 1995, **117**, 1–19.
- H. M. Aktulga, J. C. Fogarty, S. A. Pandit and A. Y. Grama, *Parallel Comput.*, 2012, **38**, 245–259.
- A. Laio and M. Parrinello, *Proc. Natl. Acad. Sci. U. S. A.*, 2002, **99**, 12562–12566.
- M. Bonomi, D. Branduardi, G. Bussi, C. Camilloni, D. Provasi, P. Raiteri, D. Donadio, F. Marinelli, F. Pietrucci and R. A. Broglia, *et al.*, *Comput. Phys. Commun.*, 2009, **180**, 1961–1972.
- J. M. Park, A. Laio, M. Iannuzzi and M. Parrinello, *J. Am. Chem. Soc.*, 2006, **128**, 11318–11319.

- 45 C. Zhang, D. G. Knyazev, Y. A. Vereshaga, E. Ippoliti, T. H. Nguyen, P. Carloni and P. Pohl, *Proc. Natl. Acad. Sci. U. S. A.*, 2012, **109**, 9744–9749.
- 46 G. Tocci and A. Michaelides, *J. Phys. Chem. Lett.*, 2014, **5**, 474–480.
- 47 G. Tocci, L. Joly and A. Michaelides, *Nano Lett.*, 2014, **14**, 6872–6877.
- 48 D. Alexeev, J. Chen, J. H. Walther, K. P. Giapis, P. Angelikopoulos and P. Koumoutsakos, *Nano Lett.*, 2015, **15**, 5744–5749.
- 49 A. R. Bizzarri and S. Cannistraro, *J. Phys. Chem. B*, 2002, **106**, 6617–6633.
- 50 N. Smolin and R. Winter, *J. Phys. Chem. B*, 2004, **108**, 15928–15937.
- 51 S. K. Sinha and S. Bandyopadhyay, *J. Chem. Phys.*, 2011, **135**, 10B602.
- 52 M. Fitzner, G. C. Sosso, S. J. Cox and A. Michaelides, *Proc. Natl. Acad. Sci. U. S. A.*, 2019, **116**, 2009–2014.
- 53 G. C. Sosso, J. Colombo, J. Behler, E. Del Gado and M. Bernasconi, *J. Phys. Chem. B*, 2014, **118**, 13621–13628.
- 54 D. N. Perera and P. Harrowell, *J. Chem. Phys.*, 1999, **111**, 5441–5454.
- 55 A. Widmer-Cooper and P. Harrowell, *J. Chem. Phys.*, 2007, **126**, 154503.